Mechanical properties of 3D printed architected polymer foams under large deformation

Huan Jiang[1+], Hannah Ziegler[1+], Zhennan Zhang[1], Han Meng[2], Dimitrios Chronopoulos[2], and Yanyu Chen[1]*

[1] Department of Mechanical Engineering, University of Louisville, Louisville, KY 40292, USA

[2] Institute for Aerospace Technology & The Composites Group, The University of Nottingham, NG7 2RD, UK

[+]These two authors contributed equally to this work.

*Corresponding author: Yanyu Chen (yanyu.chen@louisville.edu)

Abstract: Lightweight structures such as foams have gained increasing attention due to their exceptional mechanical properties, novel functionalities, and various potential applications. Traditional foams with stochastic architectures are often characterized by randomly distributed density and pore size, which makes tailoring and optimizing their mechanical performance challenging. Here we report a new type of three-dimensional architected polymer foams composed of perforated spherical shells and flat strut connectors, which can be precisely produced by 3D printing techniques. We first investigate the effects of geometric parameters, spherical thickness and flat strut slenderness, on the mechanical response of the proposed architected foams through a combined experimental and numerical methodology. We demonstrate that flat strut connectors offer unprecedented design flexibility for controlling the mechanical performance of architected foams. By tuning the geometric parameter of flat strut connectors, the stiffness of architected foams can increase about one order of magnitude while the relative density increases only by 5%. Furthermore, the failure modes can be engineered from a catastrophic one to a progressive one by using weak flat strut connectors. Our experiments elucidate the salient roles of layer by layer manufacturing process and constitutive polymer on the deformation patterns of the proposed architected foams under large deformation. The findings presented here provide useful guidelines to design polymer foams for a wide range of applications, including structures of increased crashworthiness and composite sandwich panels with enhanced vibroimpact insulation and low-velocity impact resistance.

Keywords: foam; 3D printing; architected material; printing direction; strain rate; large deformation

1. Introduction

Continuous efforts are being made to develop lightweight materials with improved stiffness, strength, and energy absorption properties for a variety of multifunctional applications [1-3]. Lightweight materials are characterized by their low density and high strength to weight ratio, making them ideal for aerospace, biomedical, semiconductor, and automotive industries. When used within automotive structures, lightweight materials can significantly improve energy efficiency [4]. Foam is a rapidly evolving lightweight structural material, which exhibits high specific strength, exceptional energy absorption, damping, and thermal properties [1,5-11]. Foams can be categorized as closed-cell or open-cell foams. Open-cell foams are characterized by the network of interconnected open pores, while closed-cell foams are the combination of individual cells separated by thin membranes [12]. Closed-cell foams have been studied widely among researchers [13-16]. However, closed-cell foams have downsides. They have underperformed compared to initial predictions due to defects that greatly reduce mechanical properties [4,17]. In addition, disconnected individual cells also limit their applications. In contrast, open-cell metallic foams have shown favorable mechanical properties under compression [18,19]. Furthermore, the high volume of interconnected porosity and large surface area make open-cell foams attractive in various applications [20-22].

Conventional foams have porosity randomly distributed within the material, taking inspiration from naturally occurring cellular structures such as bone and wood [13]. Internal geometry of random foam is described by relative density and pore size. The most common fabrication method for random metal foam is powder metallurgy [18,23-27]. This technique allows for adjustable pore sizes between 0.3 and 5 mm, and relative densities between 9 and 30%. Additionally, powder metallurgy allows for flexible material selection and is commonly used for steels, titanium, nickel, and copper. However, there are also drawbacks to this method. Bonds between sintered spheres are weak, meaning cutting the desired shape from a sintered slab of material is challenging. It is difficult to achieve complex geometries or smooth edges when cutting specimens [23]. Samples can also be molded into the desired shape before sintering. However, this method decreases sample porosity and alters the shape of hollow spheres, potentially weakening the specimen [25]. Additionally, the stochastic nature of these random foams could degrade mechanical performance in uncontrollable ways.

Architected materials with well-defined structures can be exploited to achieve tailored and unprecedented mechanical properties and functionalities. By rationally designing foam architecture on a unit cell basis, architected foams can exhibit superior and more predictable mechanical performance over random foams. Common 2D and 3D geometries, such as honeycomb and octet unit cells, have been manipulated using additive manufacturing to explore the effect of unit cell geometry and connectivity on mechanical performance [28-34]. For example, numerical and experimental studies found that polymer hybrid honeycomb structures, honeytubes, possessed superior energy absorption compared to traditional honeycombs. Coupling between failure of the two lattice designs and localized fracture resulted in sustained plateau stress for increased energy absorption [31]. Means of tailoring mechanical performance outside of the traditional method of varying relative density have also been explored for optimizing architected polymer structures without increasing weight. For example, higher stiffness was observed in 3D printed polymeric periodic structures using selective wall thickening in high stress regions to delay collapse. Additionally, it was found that varying porosity can change the deformation mode from bending to stretch-dominant, resulting in a more favorable structure [29]. Base material selection has also been explored for controlling deformation mode and mechanical properties in polymer octet truss lattices. It was found that a more rigid polymer will produce a stiffer structure with stretch-dominant behavior, while a more compliant polymer will tend toward bending-dominant due to lower solid material properties [35]. Nodal connectivity has been used as another means of controlling performance of additively manufactured polymer structures without greatly affecting weight [30,36]. It was found that pin joints and spherical joints, while similar in relative density and elastic behavior, can be selected to produce stretch-dominant and bending-dominant tensegrity-inspired structures, respectively. Additionally, buckling load and stiffness were found to increase by selecting cable and strut geometry that would facilitate bending upon compression [30]. More recently, filled 3D printed flexible polymer lattice structures have been investigated for tailored energy absorption with shape recovery by controlling internal pressure [37]. Furthermore, multifunctionality of architected polymer foams (APFs) has recently been studied. Geometric control in APF facilitates tailored and simultaneous vibroacoustic control [38,39]. APFs have also demonstrated more efficient energy absorption than metal foams and have shown an ability to recover their initial shape after large deformation [40]. Despite these design flexibilities and advanced manufacturing techniques, studies on mechanical response of architected foams under large deformation are quite limited.

In this work, the mechanical response of 3D printed APFs under large deformation is studied. By subjecting the polymer architecture to large compressive strains (70%), this research determined the energy absorption of the foams as well as elastic properties. Two unique geometric parameters, printing direction, and loading rate were found to have significant effects on mechanical properties and deformation mechanisms of the foam.

2. Materials and methods

2.1 Model design and 3D printing

The proposed APF with a body-centered cubic lattice symmetry consists of perforated spherical shells and flat strut connectors (**Figures 1 (a)** and **(b)**). The lattice constant of the representative volume element (RVE) is a. **Figure 1 (c)** shows the one-eighth of the RVE. Perforated spherical shell is characterized by external radius, R, thickness, t, and perforation radius r. Flat strut connector is described by length, l, height h, and fillet radius b, or a single parameter, binder angle θ. The binder angle θ is defined as the angle between horizontal plane and the line of sphere center and the intersection of binder and sphere, as shown in **Figure 1(c)**. In our design, the length, l, height h, and fillet radius b can all be expressed by R and θ. According to the geometric feature shown in **Figure 1 (c)**, the relative density of the proposed APF can be calculated as

$$\frac{\rho}{\rho_s}=\left(\frac{6\sqrt{3}}{25}\right)^3\left\{\frac{168\sqrt{21}\pi}{125}-8\pi\left[\frac{21}{25}-\frac{2t}{R}+\left(\frac{t}{R}\right)^2\right]^{\frac{3}{2}}-\frac{16\pi}{3}\left[\frac{3t}{R}-3\left(\frac{t}{R}\right)^2+\left(\frac{t}{R}\right)^3\right]+\frac{2\pi}{3}\left(\frac{25}{24}\tan\theta+1-\frac{25}{24\cos\theta}\right)^2\right\}+c\left(\frac{t}{R}\right)^3 \quad (1)$$

where the relation between the radius of sphere R and lattice constant a is assumed as $R = 6\sqrt{3}a/25$. The radius of the perforation is set as $r = 2R/5$ while the thickness t changes. The binder correction coefficient is defined as the correction of the volume of binder because the binder volume cannot be calculated analytically. We calculate $\pi h^2 l/4$ as the first part of binder volume, then use binder correction coefficient to correct the rest. $c = 0.027$ was determined by fitting equation (1) from CAD calculations. By changing the spherical thickness t, one can change the relative density. By changing the binder angle θ, one can tailor the shape of flat strut connectors, thereby changing the connectivity among the spherical shells. In this work, the lattice constant is set as $a = 25$ mm.

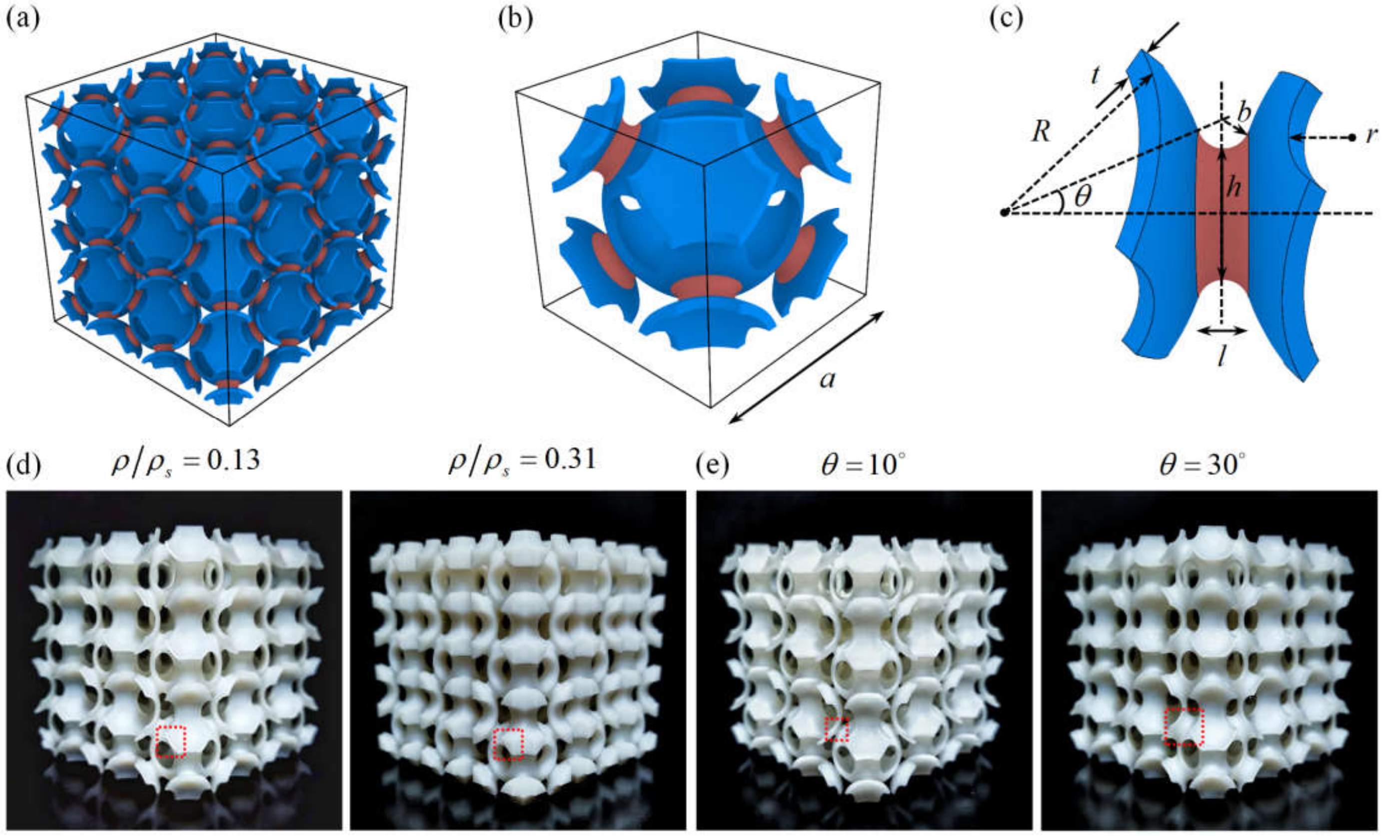

Figure 1. Design and 3D printing of 3D APFs. (a) APF foam with 3×3×3 representative volume elements (RVEs). (b) An RVE of APF. The lattice constant of the RVE is a. (c) Detailed geometric parameters for perforated spherical shell and flat strut connector. Sphere radius R, sphere thickness t, perforation radius r, binder parameter θ, and

fillet radius b. (d) 3D printed samples with $\rho/\rho_s = 0.13$ and $\rho/\rho_s = 0.31$. Here $a = 25$ mm, $r = 4t$, and $\theta = 20$. (e) 3D printed samples with $\theta = 10^\circ$ and $\theta = 30^\circ$. Here $a = 25$ mm, $t/R = 1/10$, and $r = 4t$. The dashed squares in (d) and (e) highlight the sphere thickness and size of flat strut connector, respectively.

All samples were 3D printed using Objet260 Connex3 printer (Stratasys, USA), with a printing resolution of 16 μm [41]. The micrometric sized photopolymer resin is deposited from nozzles of printer heads onto the build tray and instantly cured with UV light [42]. RGD515/531 is chosen as the base material because it is the most ductile polymer material in the printer. Printing angle is denoted as α and defined as the angle between the build layers and load direction. Specimens for testing geometric parameters and strain rate were printed with two faces parallel to the build tray, $\alpha = 0^\circ$. To vary the printing direction, samples were rotated off the horizontal to achieve the desired angle relative to the build tray. Additional support material was used on the bottom of the rotated sample to facilitate printing. After printing, samples remained on the build plate for at least two hours to completely cure. Once removed from the build plate, support material was carefully removed from perforations by using waterjet (Stratasys, USA). After that, mixed solution of sodium hydroxide and sodium metasilicate was prepared in Branson ultrasonic cleaner (Emerson Electric, USA) to dissolve the remaining support material (Sup706) in the concave side of shells. It should be pointed that due to the resolution of the printer and the technique the printer adopted, we are unable to print or unable to clean the support material of the structures with relative density under 12%. Nevertheless, our designed structures show comparable stiffness with other architected polymer foams [36,43,44], and superior to stochastic polymer foam at high relative density [41]. Printed samples with different relative densities and binder angles are shown in **Figures 1 (d)** and **(e)**, respectively.

2.2 Mechanical testing

Performance of APF was characterized by investigating the effects of geometry, printing process, and constitutive materials. Two sets of compression experiments were conducted to determine impact of geometric parameters, shell thickness and binder angle, on mechanical performance. Effects of 3D printing direction and effect of strain rate on mechanical performance were also tested. Mechanical properties determined were Young's modulus, yield strength, and energy absorption. Cubic specimens of $3\times3\times3$ RVEs were used for all experimental testing. Size of $3\times3\times3$ the specimen was selected to lessen boundary effects and keep foam yield stress below maximum force of the compression machine. Specimens were uniaxially compressed by Instron 5569A mechanical tester (Instron, USA), with a maximum load capacity of 50 kN, load resolution of 10^{-5} N, and load accuracy of $\pm0.5\%$ [45]. Load direction was perpendicular to 3D printed layers for geometry and strain rate testing. Unless otherwise specified, the compressive extension rate was controlled by the embedded software Bluehill 2.0 (Instron, USA) at 2.25 mm/min, corresponding to a compressive strain rate $5\times10^{-4}s^{-1}$. Specimens were loaded until 70% deformation, corresponding to 52.5mm deflection. Specific energy absorption was approximated using midpoint numerical integration as the area under the stress-strain curve, up to maximum deformation of 70% strain. Prior to testing, 2D Digital Image Correlation (Correlated Solutions, USA) equipment was installed to capture sample deformation. Using DIC software VIC Snap8 (Correlated Solutions, USA), focus and exposure of images were adjusted.

2.3 Finite element simulations

Finite element simulations were performed through Abaqus 6.14 (Dassault Systems, France) to provide additional insights into the deformation mechanisms of the APFs. The dynamic explicit solver with adaptive time-stepping was employed. Two sets of models, including different binder angles and different relative densities were simulated, respectively. The geometrical models were meshed using Hypermesh (Altair Engineering Inc. USA) with first-order hexahedral and second-order tetrahedral elements. The models with binder angle of 10° and 30° were meshed with 202,000 and 274,000 C3D8 elements, respectively. The model of relative density $\rho/\rho_s = 0.13$ was meshed with 217,000 C3D8 elements, and the model with relative density $\rho/\rho_s = 0.31$ was meshed with 866,000 C3D10 elements. Mesh convergence tests were performed to ensure that the number of elements is enough to capture mechanical response. For the boundary condition, the bottom face was constrained in the vertical direction. The top face was applied compressive displacement of 7.5mm, corresponding to the strain of 0.1.

A user-defined viscoplastic constitutive model was first developed to simulate the response of the 3D printed polymer in [46], where the detailed description of implementation was given. In addition, reference [47] also adopted this model and made it publicly available. In this paper, we referred to [47] for this constitutive model. The strain energy potential for the Arruda-Boyce model is [48]

$$W=\mu\left\{\frac{1}{2}(\bar{I}_1-3)+\frac{1}{20\lambda_L^2}(\bar{I}_1^2-9)+\frac{11}{1050\lambda_L^4}(\bar{I}_1^3-27)+\frac{19}{7000\lambda_L^6}(\bar{I}_1^4-81)+\frac{519}{673750\lambda_L^8}(\bar{I}_1^5-243)+\frac{K_0}{2}(\frac{J_e^2-1}{2}-\ln J_e)\right\} \tag{2}$$

where μ is the initial shear modulus, λ_L is the limiting network stretch, K_0 is the initial bulk modulus, J_e is the elastic volume ratio related to temperature. $\bar{I}_1$ is defined as [49]

$$\bar{I}_1=I_1J^{-2/3} \tag{3}$$

$$I_1=trace(\boldsymbol{B})=B_{11}+B_{22}+B_{33} \tag{4}$$

where $\boldsymbol{B}$ is left Cauchy-Green deformation tensor. The total volumetric ratio J can be described as

$$J=\sqrt{\det(\boldsymbol{B})} \tag{5}$$

If thermal effect is not considered, $J_e=J$.

The effective shear strain rate can be determined through equation [48]

$$\dot{\gamma}^p=\gamma_0\exp\left[-\frac{\Delta G}{\kappa\Theta}\left(1-\left(\frac{\sigma_e}{s}\right)^{5/6}\right)\right] \tag{6}$$

where γ_0 is the pre-exponential shear strain rate, s is the thermal shear yield strength, κ is the Boltzmann's constant, σ_e is the effective stress, ΔG is the initial free energy change.

The rate of shear yield strength for strain-softening is determined through [48]

$$\dot{s} = h\left(1 - \frac{s}{s_s}\right)\dot{\gamma}^p \tag{7}$$

where s_s is s at steady state, h is the slope of the strain-softening zone. All the parameters which contributed to this user-defined constitutive model are summarized in Table 1. Note that material failure was not considered in all simulations.

Table 1. Parameters for the user-defined constitutive model

Material parameters	Values
E (MPa)	1200
ν	0.33
γ_0	5.0×10^5
ΔG (J)	1.25×10^{-19}
s (MPa)	70
s_s (MPa)	30
h(MPa)	200
μ (MPa)	4.5
λ_L	3.5

3. Results and discussion

3.1 Effect of relative density

The first set of experiments evaluated five geometric configurations of the APF, each with a different relative density. Relative density was most influenced by shell thickness, compared to other geometric parameters. Therefore, shell thickness was varied to explore the relationship between relative density and relative stiffness. Range of relative densities was selected due to limitation on printing resolution. Stress-strain curves for relative densities ρ/ρ_s =13%, 16%, 20%, 25%, and 31% are shown in **Figure 2 (a)**. Elastic region and the first peak of each curve are shown on a separate plot for clarity in **Figure 2 (b)**. Each stress-strain curve showed an initial peak, corresponding to the first failure of each structure. Following the first failure, stress reduced, and compression continued. Stress then increased until another failure occurred. This failure process continued, evidenced by multiple peaks in the stress-strain curve until all spheres fractured. The remaining material was then compressed upon itself, known as densification, which corresponded to a rise in stress at large deformation.

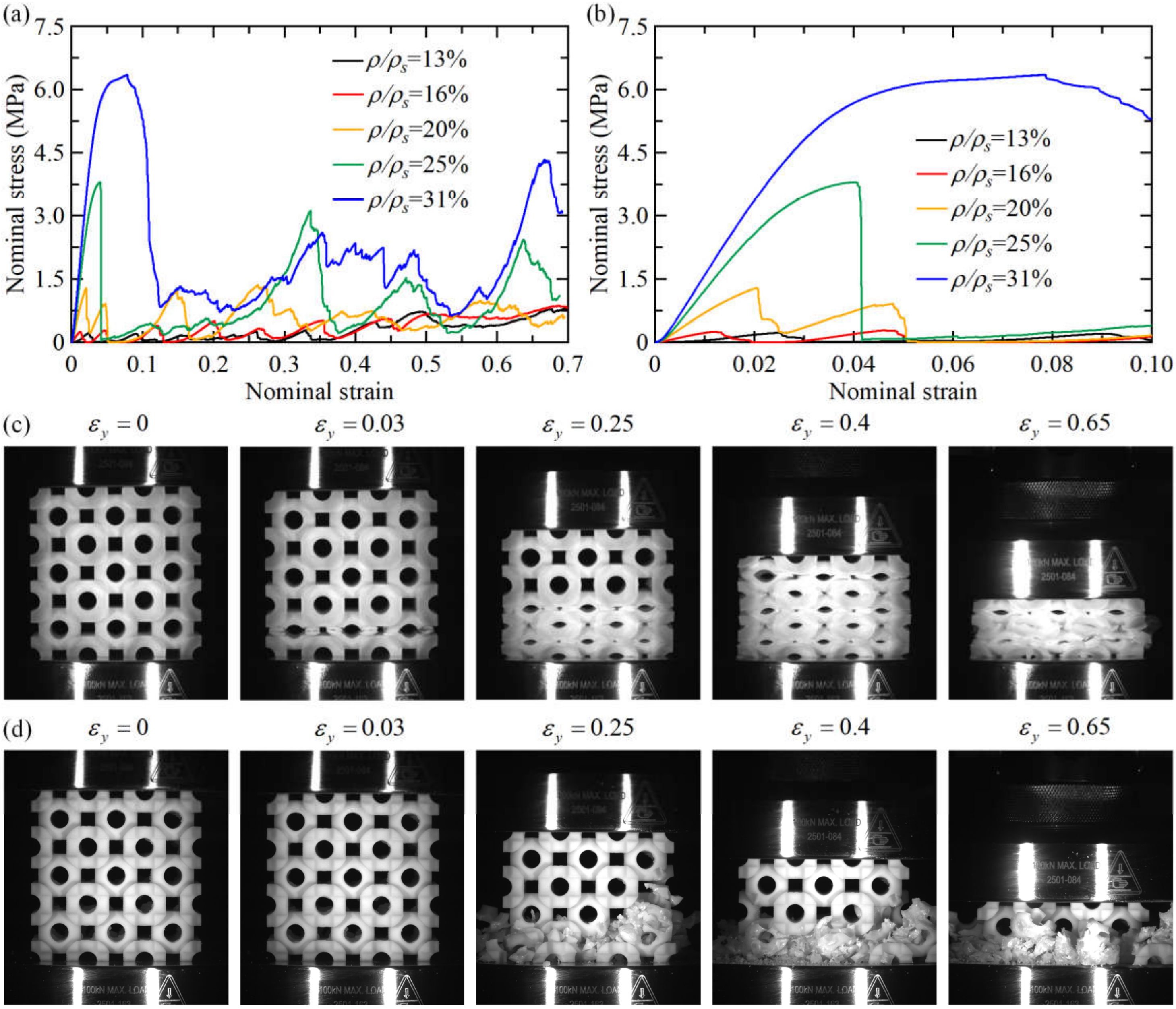

Figure 2. Effect of relative density on mechanical performance. (a)-(b) Stress-strain relations at different relative densities. (c) and (d) Deformation patterns for $\rho/\rho_s = 0.13$ and $\rho/\rho_s = 0.31$, respectively. Here $a = 25$ mm, $r = 4t$, $\theta = 20^\circ$.

Figures 2 (c)-(d) show contrasting deformation patterns for relative density $\rho/\rho_s = 13\%$ and $\rho/\rho_s = 31\%$, respectively. Deformation of $\rho/\rho_s = 13\%$ showed a progressive, layer by layer failure. Sequenced failure of layers is also visible in the stress-strain curve, with a peak corresponding to each failed layer. Following the failure of all layers, the structure was compressed further and began densification, shown as a rise in the stress-strain curve around $\varepsilon_y = 0.55$. In contrast, the deformation of $\rho/\rho_s = 31\%$ showed catastrophic failure. Stress-strain curve for $\rho/\rho_s = 31\%$ was jagged between $\varepsilon_y = 0.1$ and 0.6, with more extreme and less defined peaks compared to $\rho/\rho_s = 13\%$. Due to the randomness of the fracture position of the test, coupled with the boundary condition, failure began at the bottom of the specimen and subsequent failures occurred from bottom to top. For $\rho/\rho_s = 13\%$, first layer failure occurred at $\varepsilon_y = 0.025$, corresponding to a yield stress of 0.228 MPa. For $\rho/\rho_s = 31\%$, the first failure occurred much later, at $\varepsilon_y = 0.079$ and yield stress of 6.35 MPa. This can be verified from the second image. When $\varepsilon_y = 0.03$, the complete bottom layer has failed for $\rho/\rho_s = 13\%$, while for $\rho/\rho_s = 31\%$ structural integrity is maintained. This is because when thickness is increased, specimen tends to exhibit brittle behavior, which correspondingly will absorb more energy in the initial stage. As the strain increases to 0.65, one can observe that specimen with a relative density of 31% collapses while specimen of 13% still show some resistance against compression. This phenomenon can be attributed to the progressive failure process of 13%, the localized failure of spheres leads to the relative integrity of the model during compression compared to 31%. By contrast, the model of 31% experienced a catastrophic failure during compression, and this brittle behavior attributes to the breakdown at the strain of 0.65.

The mechanical properties including stiffness, strength, and energy absorption for the APFS are summarized in **Figure 3.** Stiffness was plotted against relative density on a log-log scale and fit with a power curve (**Figure 3(a)**). It was found that relative stiffness is related to relative density by an exponent of 2.2, indicating a bending-dominant deformation behavior. This implies that, for this architecture, varying relative density is inefficient for controlling stiffness. Yield strength and energy absorption are shown in **Figure 3 (b)** and **3 (c)**, respectively. As expected, strength and energy absorption increase with the relative density.

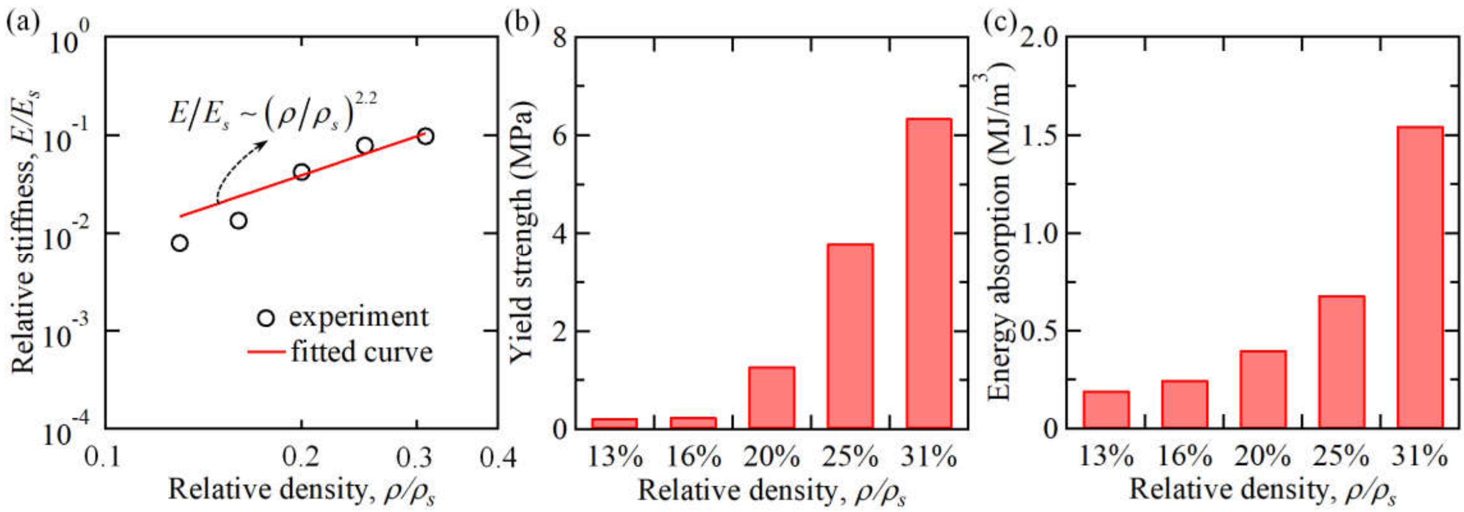

Figure 3. Effect of relative density on mechanical performance. (a) Stiffness as a function of ρ/ρ_s. (b) Strength as a function of ρ/ρ_s. (c) Energy absorption as a function of ρ/ρ_s. Here $a = 25$ mm, $r = 4t$, $\theta = 20^\circ$.

To further elucidate the deformation mechanisms, finite element simulations were performed on APFs with different relative densities. **Figure 4** shows the numerical results for APFs with $\rho/\rho_s = 13\%$ and $\rho/\rho_s = 31\%$ from $\varepsilon_y = 0$ to 0.1. For $\rho/\rho_s = 13\%$, there is no apparent peaks in the stress-strain curves, meaning this APF experiences a more stable deformation (**Figure 4 (a)**). However, for $\rho/\rho_s = 31\%$, the presence of the distinct peak in the stress-strain curve, corresponding to less uniform deformation of the structure (**Figure 4 (e)**). At the strain of 0.01, simulated contour plots reveal that stresses are concentrated on the spheres around the binders for $\rho/\rho_s = 13\%$, which leads to the yield of spheres first (**Figure 4 (b)**). But for $\rho/\rho_s = 31\%$, much of the stresses are concentrated on the binder. This indicates first yield of binders (**Figure 4 (f)**). When $\varepsilon_y = 0.03$, the stresses spread to much of the spheres, and the spheres of middle layers exhibit buckling for $\rho/\rho_s = 13\%$ (**Figure 4 (c)**). However, for $\rho/\rho_s = 31\%$, the stresses rapidly spread to most of the model and stay in a much higher stress level than that of $\rho/\rho_s = 13\%$ (**Figure 4 (g)**). At the strain of 0.08, the stresses remain fairly similar to that of $\varepsilon_y = 0.03$ for $\rho/\rho_s = 13\%$. The spheres show increased buckling, indicating a progressive deformation pattern (**Figure 4 (d)**). For $\rho/\rho_s = 31\%$, the stresses continue to spread around the model. However, one cannot observe localized spheres deformation at this stage. Instead, one can see shear deformation of binders (**Figure 4 (h)**). This indicates that failure of binders will drive the structure to catastrophic collapse, as confirmed by the experiment (**Figure 2 (d)**).

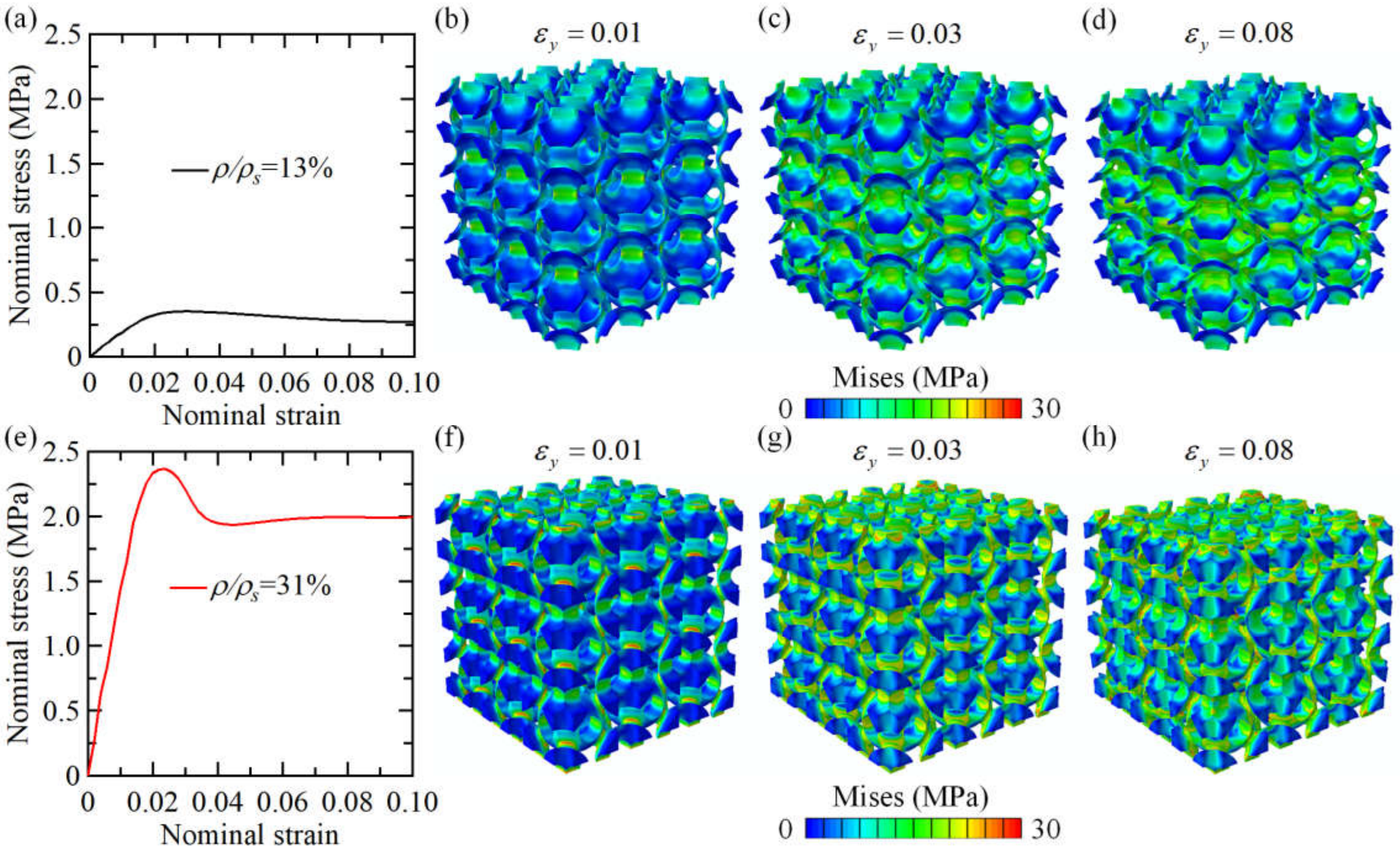

Figure 4. Finite element simulations for the mechanical response of APFs with different relative densities. (a) Simulated stress-strain curve for $\rho/\rho_s = 0.13$. (b)-(d) Simulated deformation patterns for $\rho/\rho_s = 0.13$. (e) Simulated stress-strain curve for $\rho/\rho_s = 0.31$. (f)-(h) Simulated deformation patterns for $\rho/\rho_s = 0.31$.

3.2 Effect of binder angle

Binder angle does not significantly affect relative density of the APF and was therefore tested as a unique alternative for increasing stiffness. Stress-strain curves for samples with binder angles of 10°, 20°, and 30° are shown in **Figure 5 (a)**. Each stress-strain curve shows an initial peak corresponding to first failure. Stress raised and fell for each subsequent failure. Failure continued until all spheres or binders fractured, and then densification began, shown by an increase in stress at large deformation. Young's modulus and energy absorption are shown in **Figures 5 (b)** and **5 (c)**, respectively. It is shown that Young's modulus and energy absorption increased with binder angle. In contrast to increasing shell thickness, increasing binder angle has little effect on relative density of the structure. By increasing binder angle from $\theta = 10^\circ$ to $\theta = 30^\circ$, stiffness increased over an order of magnitude, while relative density only increased by 5%. With the ability to vastly increase stiffness without greatly increasing weight, binder angle is much more efficient for improving mechanical properties than wall thickness. In this sense, binder angle could be used to design efficient graded structures with controllable deformation patterns and mechanical properties.

Figures 5 (d)-(e) shows contrasting deformation patterns for binder angles 10° and 30°, respectively. Deformation of $\theta = 10^\circ$ showed progressive failure, which can be observed from **Figure 5 (d)**, similar to $\rho/\rho_s = 0.13$ at $\theta = 20^\circ$ in **Figure 2 (c)**. Following layer by layer failure, densification gradually started around $\varepsilon_y = 0.6$. For $\theta = 30^\circ$, however, the structure experienced a catastrophic failure. The stress-strain curve showed less defined peaks after $\varepsilon_y = 0.2$, evidenced by non-uniform deformation in images of $\varepsilon_y = 0.25$ to 0.65. First failure of $\theta = 10^\circ$ occurred at $\varepsilon_y = 0.039$ with a yield stress of 0.075 MPa. In contrast, first failure of $\theta = 30^\circ$ began much earlier with $\varepsilon_y = 0.02$ and yield stress of 0.525 MPa. This can be observed from the second image of **Figure 5 (d) and (e)** where the bottom layer of $\theta = 30^\circ$ failed at $\varepsilon_y = 0.024$, while $\theta = 10^\circ$ remained intact.

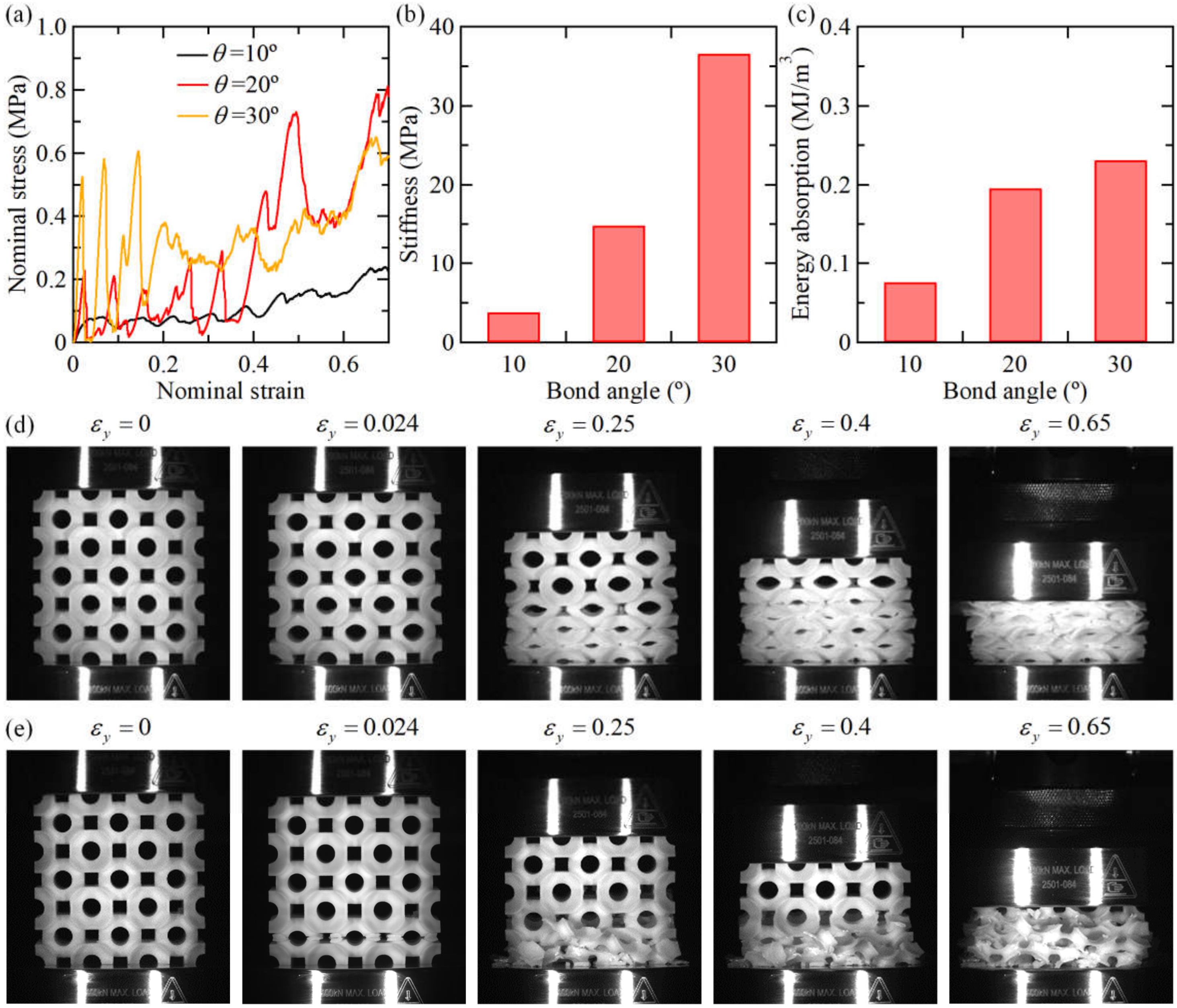

Figure 5. Effect of binder angle on mechanical performance. (a) Stress-strain relations for $\theta = 10^\circ$, $\theta = 20^\circ$, and $\theta = 30^\circ$. (b) Stiffness. (c) Energy absorption. (d) and (e) Deformation patterns for $\theta = 10^\circ$ and $\theta = 30^\circ$, respectively. Here a = 25 mm, $\rho/\rho_s = 0.13$, $r = 4t$.

Our simulation results are shown in **Figure 6**. We have calibrated our simulation based on the model with a relative density of 13%. The calibration revealed that simulation result is consistent with experimental result for printing direction of 90° while higher than the printing direction of 0°. This is because the mechanical behavior is dependent on printing direction and the possible imperfections involved during printing. In our simulation, we did not consider the anisotropic feature and failure. It should be pointed out that the purpose of the numerical simulation in this work is to provide additional information to identify the deformation mechanisms.

Figure 6 shows the numerical simulation results for APFs with $\theta = 10^{\circ}$ and $\theta = 30^{\circ}$, respectively. For $\theta = 10^{\circ}$, there is no distinct peak on the stress-strain curve, indicating a stable deformation (**Figure 6 (a)**). In contrast, the presence of apparent stress peak for $\theta = 30^{\circ}$ indicates a less uniform deformation (**Figure 6 (e)**). At the strain of 0.01, it can be observed that the stresses are concentrated on the binders and part of the spheres around binders for $\theta = 10^{\circ}$ (**Figure 6 (b)**). For $\theta = 30^{\circ}$, the stresses are concentrated on local spheres around the binders and the stress level is higher than that of $\theta = 10^{\circ}$ (**Figure 6 (f)**). When $\varepsilon_y = 0.024$, stresses are locally concentrated on the interface of different layers for $\theta = 10^{\circ}$. This leads to yield and buckling of spheres in the middle layer (**Figure 6 (c)**). However, for $\theta = 30^{\circ}$, the stresses spread to most of the model from $\varepsilon_y = 0.01$ to 0.024. This indicates that binder of $\theta = 30^{\circ}$ functions much more efficiently with regard to transferring stresses from binder to sphere compared with $\theta = 10^{\circ}$. The high-stress transfer efficiency means that a more uniform stress distribution can be expected for $\theta = 30^{\circ}$ (**Figure 6 (g)**). The uniform stress distribution drives the APF to a catastrophic failure mode, as confirmed from experiment (**Figure 5 (e)**).

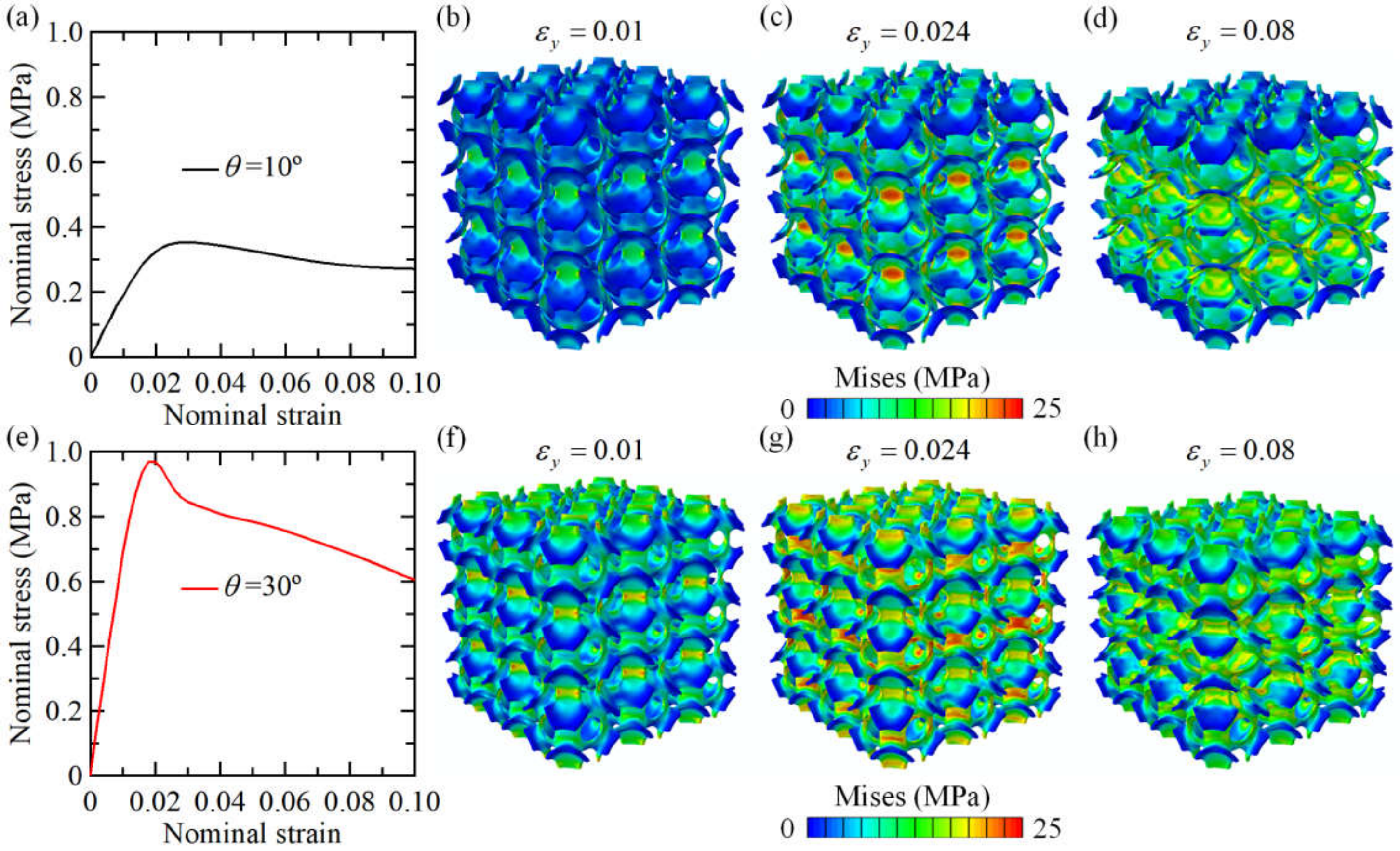

Figure 6. Finite element simulations for the mechanical response of APFs with different binder angles. (a) Simulated stress-strain curve for $\theta = 10^{\circ}$. (b)-(d) Simulated deformation patterns for $\theta = 10^{\circ}$. (e) Simulated stress-strain curve for $\theta = 30^{\circ}$. (f)-(h) Simulated deformation patterns for $\theta = 30^{\circ}$.

3.3 Effect of printing direction

To understand the effect of manufacturing process on the mechanical performance of APFs, samples were 3D printed at different orientations to the build tray. Stress-strain curves for samples printed at $\alpha = 0^{\circ}$, 15°, 30°, 45°, 60°, 75° and 90° are shown in **Figure 7 (a)**. Elastic region and first peak of each curve are shown on a separate plot for clarity in **Figure 7 (b)**. Stress-strain curves for all orientations showed different peaks, meaning structures failed in multiple stages. Several stress peaks existed in all curves, but peaks became less as print angle increased. Failure continued in the structure until all spheres fractured, and then stress increased as densification occurred.

Figures 7 (c)-(e) show deformation patterns for $\alpha = 15^{\circ}$, $\alpha = 45^{\circ}$, and $\alpha = 75^{\circ}$, respectively. Deformation of $\alpha = 15^{\circ}$ showed progressive failure. First failure occurred along the printing direction at $\varepsilon_y = 0.027$ with a yield stress of 0.315 MPa. Failure began at the top of the structure at $\varepsilon_y = 0.15$, and propagated along printing direction of 15°. This is expected due to the comparatively weak bonding interface during the layer-by-layer fabrication. Then, failure occurred in other layers, and not sequentially. This verified the randomness of the failure position because the specimen was symmetric. Finally, well-defined densification can be observed at $\varepsilon_y = 0.6$. In contrast, for $\alpha = 45^{\circ}$ and $\alpha = 75^{\circ}$, much more pronounced effect of printing direction can be observed. First failure occurred at $\varepsilon_y = 0.033$ and $\varepsilon_y = 0.017$ for $\alpha = 45^{\circ}$ and $\alpha = 75^{\circ}$, respectively. At $\varepsilon_y = 0.05$, both models exhibited clear fractures along printing direction, especially for $\alpha = 75^{\circ}$. When compressed to the $\varepsilon_y = 0.15$, $\alpha = 45^{\circ}$ showed a clear shear band of 45°, followed by the failure along with the shear band. After the shear band failed, the remaining part was compressed until the end of the experiment. For $\alpha = 75^{\circ}$, one may not observe shear band as distinct as $\alpha = 45^{\circ}$ at $\varepsilon_y = 0.15$. However, some parts of the spheres break until disconnected along 75°, and this trend continued to grow to the end of the test. As a result, samples collapsed, and no significant densification can be observed at $\varepsilon_y = 0.6$ for these two cases. Intrinsically, this is attributed to the weak bonding of interface between layers. Failure becomes much more drastic with the increase of the printing direction, especially at relatively large deformation. This is also evidenced by the less defined peaks when the printing angle increases.

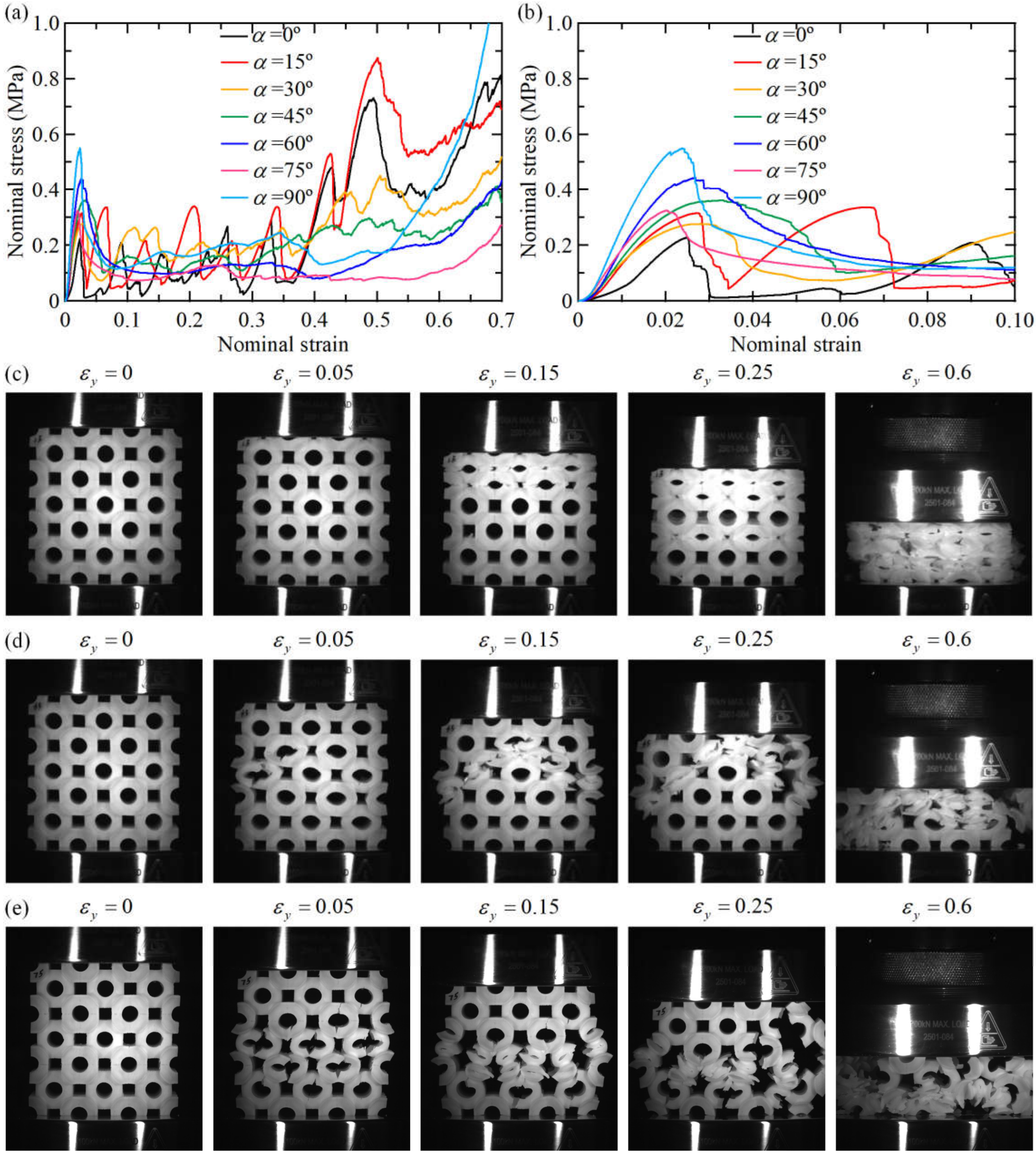

(a)
Nominal stress (MPa)
Nominal strain
α =0°
α =15°
α =30°
α =45°
α =60°
α =75°
α =90°
(b)
Nominal stress (MPa)
Nominal strain
α =0°
α =15°
α =30°
α =45°
α =60°
α =75°
α =90°
(c)
(d)
(e)
$\varepsilon_y = 0$
$\varepsilon_y = 0.05$
$\varepsilon_y = 0.15$
$\varepsilon_y = 0.25$
$\varepsilon_y = 0.6$

Figure 7. Effect of printing direction on mechanical performance. (a)-(b) Stress-strain curves for different printing directions. (c)-(e) Deformation patterns for $\alpha = 15^{\circ}$, $\alpha = 45^{\circ}$, and $\alpha = 75^{\circ}$, respectively.

Figures 8 (a)-(c) show Young's modulus, yield strength, energy absorption of APFs for different printing directions, respectively. It is shown that the stiffness and strength increase with the printing angle. From heuristic point of view, composite ply theory can be applied to explain this phenomenon. Take lamina as an example, plies are the different layers the printer has printed. Assume vertical load of P, the load applied along the fiber direction will be $P\sin\alpha$. This means that for $\alpha = 90^{\circ}$, the load is all applied along the stiffest fiber direction. However, for $\alpha = 0^{\circ}$, load is applied to the weakest direction which is perpendicular to fiber. Other printing direction follows the same principle. Energy absorption was highest for $\alpha = 15^{\circ}$ and decreased with increasing α, as failure became less stable, until $\alpha = 90^{\circ}$.

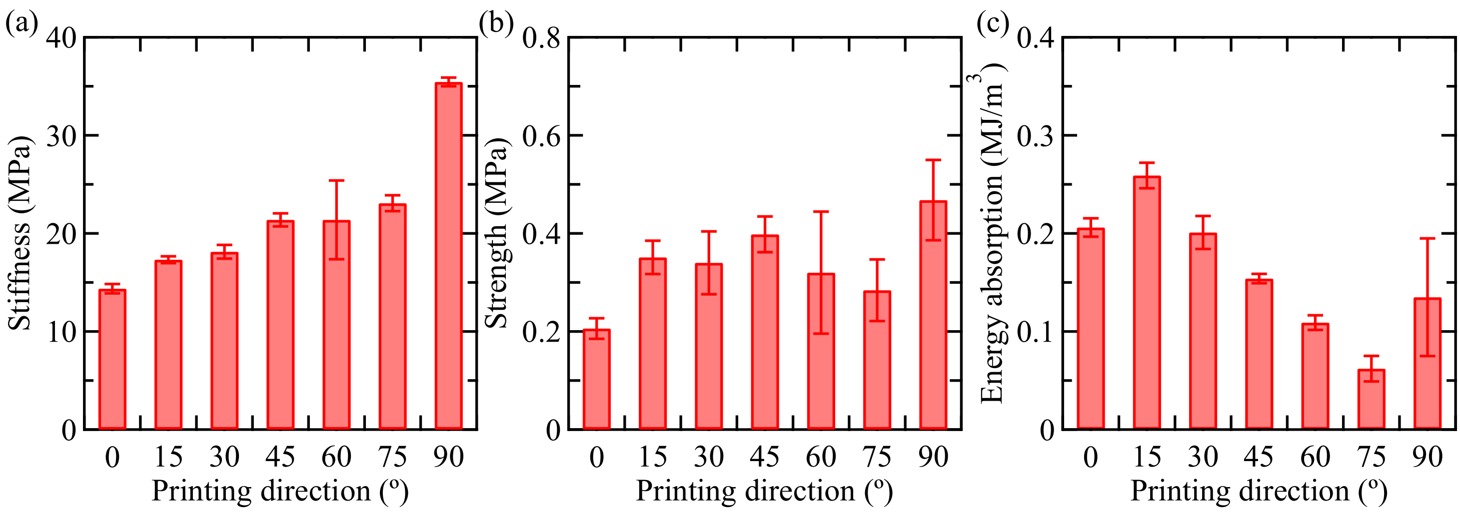

Figure 8. Effect of printing direction on mechanical performance. (a) Stiffness as a function of α. (b) Strength as a function of α. (c) Energy absorption as a function of α. Here $a = 25$ mm, $t/R = 1/10$, $r = 4t$, $\theta = 20^{\circ}$.

3.4 Effect of loading rate

Depending on the application of APFs, the structure may be subjected to different loading rates. Five strain rates were tested on the same geometry to understand the effect of loading rate on mechanical response and failure modes. Stress-strain curves for samples subjected to strain rates 0.1, 0.01, 0.001, 0.0005, and 0.00001 s^{-1} are shown in **Figure 9 (a)**. Elastic region and first peak of each curve are shown on a separate plot for clarity in **Figure 9 (b)**. Each stress-strain curve showed an initial peak, corresponding to first failure of each structure. Multiple peaks existed for all stress-strain curves, corresponding to a layer failure. Notably, peaks became increasingly less as strain rate increased. Deformation continued in each structure until all spheres fractured, followed by densification.

Figures 9 (c) and **(d)** show deformation patterns for strain rates 0.1 and 0.00001 s^{-1}, respectively. Deformation at a strain rate of 0.1 s^{-1} showed a non-uniform and catastrophic failure. The first failure occurred at $\varepsilon_y = 0.03$, corresponding to a yield stress of 0.645 MPa. Failure began in the middle layer of the specimen. Initial failure was less uniform throughout the layer than other stable layer failures, resulting in loss of small fragments. As seen in the image at $\varepsilon_y = 0.07$, the failed layer was compressed until another failure occurred due to insufficient time to further absorb energy. At $\varepsilon_y = 0.14$, the second failure was not contained within one layer of the structure but spanned multiple layers surrounding the first failed layer. Collapsed spheres created an angled deformation band from the bottom left corner of the specimen to the middle right. Partial failure of layers resulted in continued non-uniform collapse. Material was contained within the initial profile and the top layer had not fractured for $\varepsilon_y = 0.22$. The APF compressed at a strain rate of 0.00001 s^{-1}, however, showed a stable and progressive collapse. Different from the fragmented collapse of the APF at 0.1 s^{-1} strain rate, no obvious cracks can be seen at $\varepsilon_y = 0.03$. Failure began in the middle layer at $\varepsilon_y = 0.07$ and continued in other layers. At $\varepsilon_y = 0.22$, material was well contained within the structure and deformation was visible in all layers, showing a stable failure mode.

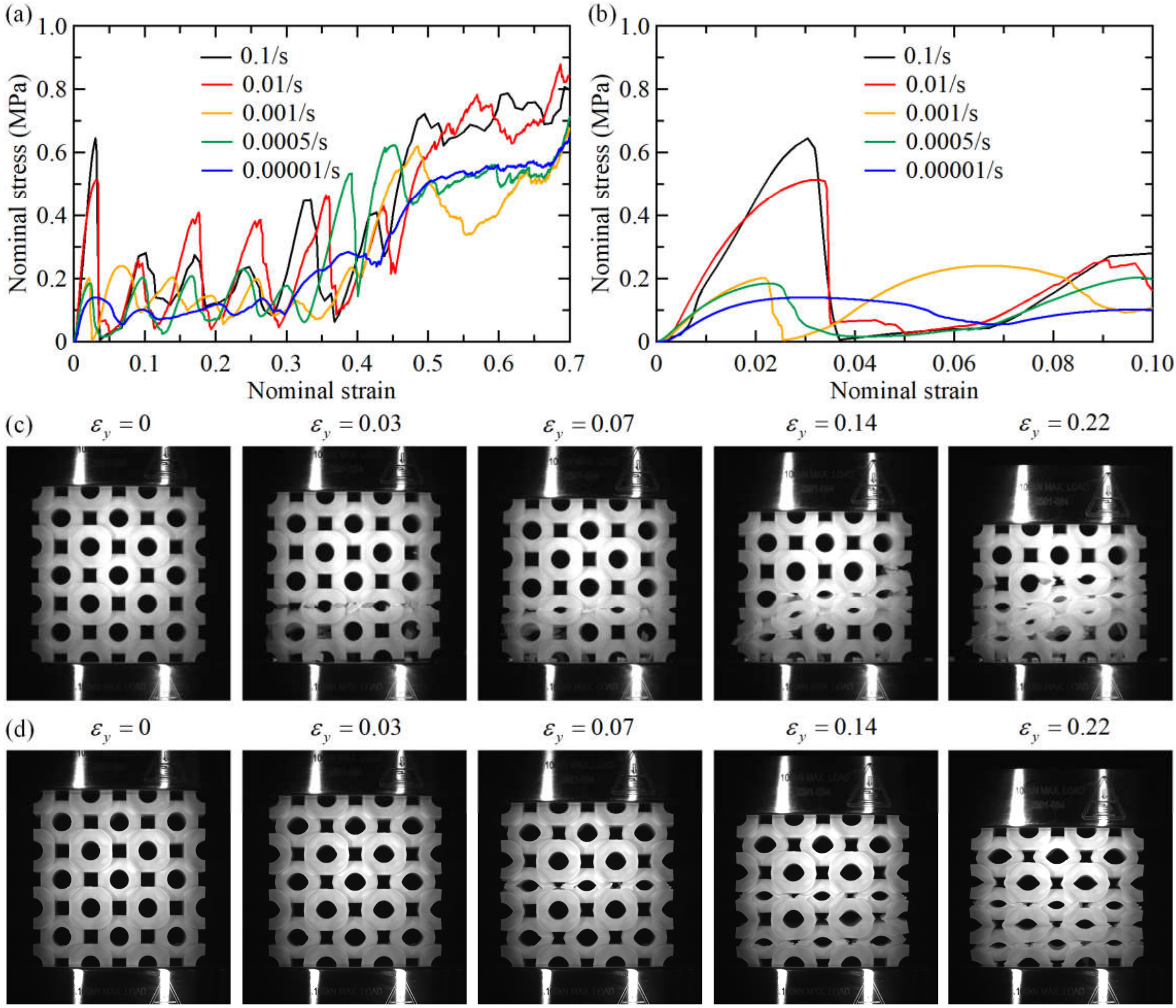

Figure 9. Effect of loading rate from 10^{-5} to 0.1/s. (a)-(b) Stress-strain curves for $\dot{\varepsilon}=10^{-5}$, $\dot{\varepsilon}=10^{-4}$, $\dot{\varepsilon}=10^{-3}$, $\dot{\varepsilon}=10^{-2}$, and $\dot{\varepsilon}=10^{-1}$. (c) Deformation patterns for a strain rate of $\dot{\varepsilon}=10^{-1}$, and (d) Deformation patterns for a strain rate of $\dot{\varepsilon}=10^{-5}$. Here a = 25 mm, $t/R=1/10$, $r=4t$, θ = 20°.

Stiffness, strength, and energy absorption were obtained from stress-strain curves for strain rates of 0.1, 0.01, 0.001, 0.0005, and 0.00001 s^{-1} are shown in **Figures 10 (a)-(c)**, respectively. Two trials were performed for each strain rate. Averages are reported in **Figure 10**, with deviation lines indicating results from each trial. It is shown that stiffness increases with increasing strain rate, but the three lowest rates result in similar stiffness values. Yield strength is consistent for three lowest strain rates but increases at higher strain rates. This indicates that mechanical behavior of APFs is not highly influenced by low strain rates. Yield strength for highest strain rate was over three times that of the lowest strain rate. Therefore, effect of loading rate on stiffness and strength is evident in the two highest strain rates, which are above standard quasi-static rates [50]. This improved mechanical properties at high loading rates can be attributed to stiffer molecular chains which are reoriented within the base material [51]. Energy absorption is fairly constant for all strain rates, with a slight increase at higher loading rates. This study provides a preliminary investigation into strain rate dependent mechanical performance of 3D printed structures. Further tests at higher strain rates need to be performed to understand the dynamic response of the proposed APFs.

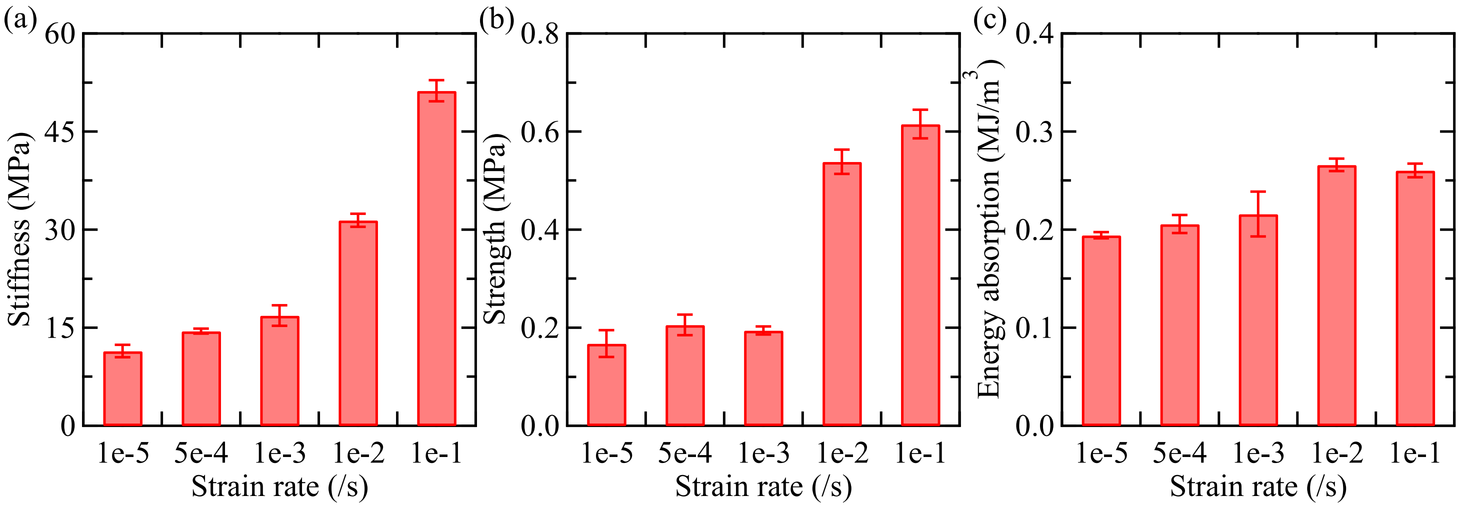

Figure 10. Effect of strain rate on mechanical performance. (a) Stiffness as a function of strain rate. (b) Strength as a function of strain rate. (c) Energy absorption as a function of strain rate. Here $a = 25$ mm, $t/R = 1/10$, $r = 4t$, $\theta = 20^\circ$.

4. Conclusions

This paper demonstrated successful 3D printing and testing of a novel APF with engineered mechanical performance. Mechanical properties improved with increasing relative density, but foam architecture was observed to be bending-dominant. Increasing the relative density of the structure was inefficient for controlling stiffness, due to the bending-dominant behavior. The influence of the binder angle was investigated as an alternative for tailoring the effective stiffness of the APF. Increasing the binder angle greatly increased stiffness with little effect on relative density. Varying the binder size altered the stress transfer path of the structure, rendering the binder angle a more effective parameter for controlling stiffness. This implies that the binder angle could be used to design graded structures with controllable mechanical performance. In addition to geometric parameters, the printing process had a large impact on mechanical performance. Structures fractured along the print direction and mechanical properties were superior when loaded parallel to printed layers. Moreover, the mechanical performance of APF was strain rate dependent due to the rate sensitivity of the base material. It should be pointed out that the strain rate tested here is still very low, which cannot represent extreme dynamic loading conditions. Exending the strain rate to higher levels will be essiential to examine the effectiveness of architected foams employed in blast and impact protection systems. In addition, the finite element simulations performed here cannot consider the layer-by-layer feature of the printed samples and manufacturing defects involved. This can be resolved by improving the current constitutive model to incorporate anisotropy and failure criteria. Nevertheless, the findings presented here can provide design guidelines for engineering open-cell foam structures to be employed within a wide range of applications, including structures of increased crashworthiness and composite sandwich panels, with enhanced vibroimpact insulation and low-velocity impact resistance.

Acknowledgments

Y. Chen gratefully acknowledges the start-up fund from the Department of Mechanical Engineering at the University of Louisville.

Data availability

The raw/processed data required to reproduce these findings cannot be shared at this time due to legal or ethical reasons. Data are however available from the authors upon reasonable request.

References

[1] W. Sanders, L. Gibson, Mechanics of BCC and FCC hollow-sphere foams, Materials Science and Engineering: A. 352 (1-2) (2003) 150-161.

[2] C. Bonatti, D. Mohr, Large deformation response of additively-manufactured FCC metamaterials: From octet truss lattices towards continuous shell mesostructures, International Journal of Plasticity. 92 (2017) 122-147.

[3] O. Caty, E. Maire, T. Douillard, P. Bertino, R. Dejaeger, R. Bouchet, Experimental determination of the macroscopic fatigue properties of metal hollow sphere structures, Materials Letters. 63 (13-14) (2009) 1131-1134.

[4] W.S. Sanders, Mechanical behavior of closed-cell and hollow-sphere metallic foams, Journal. (Issue) (2002).

[5] T. Fiedler, A. Öchsner, On the anisotropy of adhesively bonded metallic hollow sphere structures, Scripta materialia. 58 (8) (2008) 695-698.

[6] K. Boomsma, D. Poulikakos, F. Zwick, Metal foams as compact high performance heat exchangers, Mechanics of materials. 35 (12) (2003) 1161-1176.

[7] S.-T. Hong, D.R. Herling, Open-cell aluminum foams filled with phase change materials as compact heat sinks, Scripta Materialia. 55 (10) (2006) 887-890.

[8] W.S. Sanders, L. Gibson, Mechanics of hollow sphere foams, Materials Science and Engineering: A. 347 (1-2) (2003) 70-85.

[9] N. Mills, C. Fitzgerald, A. Gilchrist, R. Verdejo, Polymer foams for personal protection: cushions, shoes and helmets, Composites science and technology. 63 (16) (2003) 2389-2400.

[10] K. Ahuja, J. Gaeta, R, K. Ahuja, J. Gaeta, R, A new wide-band acoustic liner with high temperature capability, Journal. (Issue) (1997) 1701.

[11] S. Babaee, P. Wang, K. Bertoldi, Three-dimensional adaptive soft phononic crystals, Journal of Applied Physics. 117 (24) (2015) 244903.

[12] T. Bleistein, M. Reis, X. Cheng, C. Redenbach, S. Diebels, A. Jung, Multiscale microsphere modelling of open-cell metal foams enriched by statistical analysis of geometric parameters, Mechanics of Materials. 142 (2020) 103295.

[13] A.P. Roberts, E.J. Garboczi, Elastic moduli of model random three-dimensional closed-cell cellular solids, Acta materialia. 49 (2) (2001) 189-197.

[14] W.-Y. Jang, W.-Y. Hsieh, C.-C. Miao, Y.-C. Yen, Microstructure and mechanical properties of ALPORAS closed-cell aluminium foam, Materials Characterization. 107 (2015) 228-238.

[15] I. Jeon, T. Asahina, The effect of structural defects on the compressive behavior of closed-cell Al foam, Acta materialia. 53 (12) (2005) 3415-3423.

[16] M. Kader, M. Islam, M. Saadatfar, P. Hazell, A. Brown, S. Ahmed, J. Escobedo, Macro and micro collapse mechanisms of closed-cell aluminium foams during quasi-static compression, Materials & Design. 118 (2017) 11-21.

[17] O. Friedl, C. Motz, H. Peterlik, S. Puchegger, N. Reger, R. Pippan, Experimental investigation of mechanical properties of metallic hollow sphere structures, Metallurgical and Materials Transactions B. 39 (1) (2008) 135-146.

[18] R. Kumar, H. Jain, S. Sriram, A. Chaudhary, A. Khare, V.A. Ch, D. Mondal, Lightweight open cell aluminum foam for superior mechanical and electromagnetic interference shielding properties, Materials Chemistry and Physics. 240 (2020) 122274.

[19] A. Mamalis, D. Manolakos, M. Ioannidis, D. Chronopoulos, P. Kostazos, On the crashworthiness of composite rectangular thin-walled tubes internally reinforced with aluminium or polymeric foams: Experimental and numerical simulation, Composite Structures. 89 (3) (2009) 416-423.

[20] O. Kesler, L.K. Crews, L.J. Gibson, Creep of sandwich beams with metallic foam cores, Materials Science and Engineering: A. 341 (1) (2003) 264-272.
[21] K. Li, X.-L. Gao, Micromechanical Modeling of Three-dimensional Open-cell Foams, Advances in Soft Matter Mechanics, Springer2012, pp. 213-258.
[22] K. Li, X.-L. Gao, A. Roy, Micromechanical modeling of three-dimensional open-cell foams using the matrix method for spatial frames, Composites part B: engineering. 36 (3) (2005) 249-262.
[23] S. Szyniszewski, B. Smith, J. Hajjar, B. Schafer, S. Arwade, The mechanical properties and modeling of a sintered hollow sphere steel foam, Materials & Design (1980-2015). 54 (2014) 1083-1094.
[24] A. Taşdemirci, Ç. Ergönenç, M. Güden, Split Hopkinson pressure bar multiple reloading and modeling of a 316 L stainless steel metallic hollow sphere structure, International journal of impact engineering. 37 (3) (2010) 250-259.
[25] T. Fiedler, C. Veyhl, I. Belova, T. Bernthaler, B. Heine, G. Murch, Mechanical properties and micro-deformation of sintered metallic hollow sphere structure, Computational materials science. 74 (2013) 143-147.
[26] A. Sutygina, U. Betke, M. Scheffler, Open-Cell Aluminum Foams by the Sponge Replication Technique: A Starting Powder Particle Study, Advanced Engineering Materials. (2020) 1901194.
[27] P. Lhuissier, A. Fallet, L. Salvo, Y. Brechet, Quasistatic mechanical behaviour of stainless steel hollow sphere foam: Macroscopic properties and damage mechanisms followed by X-ray tomography, Materials Letters. 63 (13-14) (2009) 1113-1116.
[28] M. Xu, Z. Xu, Z. Zhang, H. Lei, Y. Bai, D. Fang, Mechanical properties and energy absorption capability of AuxHex structure under in-plane compression: Theoretical and experimental studies, International Journal of Mechanical Sciences. 159 (2019) 43-57.
[29] H. Jia, H. Lei, P. Wang, J. Meng, C. Li, H. Zhou, X. Zhang, D. Fang, An experimental and numerical investigation of compressive response of designed Schwarz Primitive triply periodic minimal surface with non-uniform shell thickness, Extreme Mechanics Letters. (2020) 100671.
[30] K. Pajunen, P. Johanns, R.K. Pal, J.J. Rimoli, C. Daraio, Design and impact response of 3D-printable tensegrity-inspired structures, Materials & Design. 182 (2019) 107966.
[31] J. Xu, Y. Wu, L. Wang, J. Li, Y. Yang, Y. Tian, Z. Gong, P. Zhang, S. Nutt, S. Yin, Compressive properties of hollow lattice truss reinforced honeycombs (Honeytubes) by additive manufacturing: patterning and tube alignment effects, Materials & Design. 156 (2018) 446-457.
[32] F. Usta, F. Scarpa, H.S. Türkmen, CORONAEdgewise compression of novel hexagonal hierarchical and asymmetric unit cells honeycomb metamaterials, Materials Today Communications. (2020) 101102.
[33] S. Hou, T. Li, Z. Jia, L. Wang, Mechanical properties of sandwich composites with 3d-printed auxetic and non-auxetic lattice cores under low velocity impact, Materials & Design. 160 (2018) 1305-1321.
[34] H. Yang, B. Wang, L. Ma, Designing hierarchical metamaterials by topology analysis with tailored Poisson's ratio and Young's modulus, Composite Structures. 214 (2019) 359-378.
[35] M. Kaur, T.G. Yun, S.M. Han, E.L. Thomas, W.S. Kim, 3D printed stretching-dominated micro-trusses, Materials & Design. 134 (2017) 272-280.
[36] Z. Vangelatos, K. Komvopoulos, J. Spanos, M. Farsari, C. Grigoropoulos, Anisotropic and curved lattice members enhance the structural integrity and mechanical performance of architected metamaterials, International Journal of Solids and Structures. 193 (2020) 287-301.
[37] Y. Wang, B. Ramirez, K. Carpenter, C. Naify, D.C. Hofmann, C. Daraio, Architected lattices with adaptive energy absorption, Extreme Mechanics Letters. 33 (2019) 100557.
[38] O. McGee, H. Jiang, F. Qian, Z. Jia, L. Wang, H. Meng, D. Chronopoulos, Y. Chen, L. Zuo, 3D printed architected hollow sphere foams with low-frequency phononic band gaps, Additive Manufacturing. 30 (2019) 100842.
[39] H. Jiang, Y. Chen, Lightweight architected hollow sphere foams for simultaneous noise and vibration control, Journal of Physics D: Applied Physics. 52 (32) (2019) 325303.
[40] M. Mohsenizadeh, F. Gasbarri, M. Munther, A. Beheshti, K. Davami, Additively-manufactured lightweight Metamaterials for energy absorption, Materials & Design. 139 (2018) 521-530.

[41] M. Tarantino, O. Zerhouni, K. Danas, Random 3D-printed isotropic composites with high volume fraction of pore-like polydisperse inclusions and near-optimal elastic stiffness, Acta Materialia. 175 (2019) 331-340.
[42] S. Kramer, J.L. Jordan, H. Jin, J. Carroll, A.M. Beese, Mechanics of Additive and Advanced Manufacturing, Volume 8: Proceedings of the 2018 Annual Conference on Experimental and Applied Mechanics, Springer2018.
[43] Y. Duan, B. Du, X. Shi, B. Hou, Y. Li, Quasi-static and dynamic compressive properties and deformation mechanisms of 3D printed polymeric cellular structures with Kelvin cells, International Journal of Impact Engineering. 132 (2019) 103303.
[44] C.W. Visser, D.N. Amato, J. Mueller, J.A. Lewis, Architected Polymer Foams via Direct Bubble Writing, Advanced materials. 31 (46) (2019) 1904668.
[45] Instron, Instron 5569 Load Frame Manual, (2008).
[46] P. Zhang, A.C. To, Transversely isotropic hyperelastic-viscoplastic model for glassy polymers with application to additive manufactured photopolymers, International Journal of Plasticity. 80 (2016) 56-74.
[47] L. Liu, A Triaxiality-Dependent Constitutive Model For Predicting Damage-Induced Softening in 3D-Printed Soft Suture Layer, (2018).
[48] E.M. Arruda, M.C. Boyce, A three-dimensional constitutive model for the large stretch behavior of rubber elastic materials, (1993).
[49] A. Documentation, (2014).
[50] X. Yang, H. Yang, Z. Lai, S. Zhang, Dynamic tensile behavior of S690 high-strength structural steel at intermediate strain rates, Journal of Constructional Steel Research. 168 (2020) 105961.
[51] M.C. Boyce, D.M. Parks, A.S. Argon, Large inelastic deformation of glassy polymers. Part I: rate dependent constitutive model, Mechanics of materials. 7 (1) (1988) 15-33.